ANNUAL REVIEWS

Annual Review of Biophysics

Raman Imaging of Small Biomolecules

Yihui Shen, Fanghao Hu, and Wei Min

Department of Chemistry, Columbia University, New York, NY 10027, USA;
email: wm2256@columbia.edu

Annu. Rev. Biophys. 2019. 48:347–69

First published as a Review in Advance on March 20, 2019

The *Annual Review of Biophysics* is online at biophys.annualreviews.org

https://doi.org/10.1146/annurev-biophys-052118-115500

Keywords

Raman microscopy, small molecule imaging, vibrational tags, lipid metabolism, drug imaging

Abstract

Imaging techniques greatly facilitate the comprehensive knowledge of biological systems. Although imaging methodology for biomacromolecules such as protein and nucleic acids has been long established, microscopic techniques and contrast mechanisms are relatively limited for small biomolecules, which are equally important participants in biological processes. Recent developments in Raman imaging, including both microscopy and tailored vibrational tags, have created exciting opportunities for noninvasive imaging of small biomolecules in living cells, tissues, and organisms. Here, we summarize the principle and workflow of small-biomolecule imaging by Raman microscopy. Then, we review recent efforts in imaging, for example, lipids, metabolites, and drugs. The unique advantage of Raman imaging has been manifested in a variety of applications that have provided novel biological insights.

Contents

THE NEED FOR IMAGING SMALL BIOMOLECULES

Biological systems are by no means simple, random mixtures of molecules. Heterogeneity exists across different length scales, reflecting the hierarchical organization in a complex system. At the tissue level (above 100 μm), different cell types are spatially intermixed; nutrients in the bloodstream might not permeate the entire tissue with the same efficiency. At the cellular level (10 ∼ 100 μm), gene expression and epigenetic regulation could vary dramatically among different cell types and cell states. At the subcellular level (0.1 ∼ 10 μm), a protein could be guided to a specific organelle by its localization signal; chemical gradient could be generated as a result of membrane compartmentalization or molecular affinity binding. Therefore, in our efforts toward a holistic understanding of how life functions, in addition to learning what the individual components are, it becomes equally important to know where they are in space and how they respond to dynamic changes. Consequently, the increasing demand for such spatiotemporal information has driven the development of imaging techniques with the ability to resolve these components and their interactions.

Joint efforts to develop instrumentation and contrast mechanism, two key components comprising an imaging methodology, have revolutionized imaging techniques. Fluorescence imaging of specific biomacromolecules such as proteins and nucleic acids is a perfect manifestation. For example, intracellular proteins can be visualized by binding with dye-labeled antibodies, or by tagging with genetically encoded green fluorescent protein (GFP) or hybrid protein-chemical tags (80). The specific sequence of nucleic acids can be visualized by their complementary chains, as in fluorescence in situ hybridization (FISH) (55) and clustered regularly interspaced short

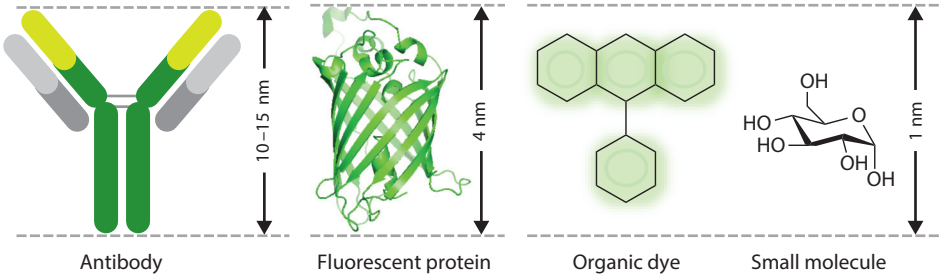

Figure 1

Intuitive size comparison between IgG antibody (10–15 nm), GFP (about 4 nm), organic fluorescent dye (about 1 nm), and a typical small biomolecule (glucose) (less than 1 nm) at the indicated scale. Abbreviation: GFP, green fluorescent protein.

palindromic repeats (CRISPR) imaging (13), or by attaching a fluorophore-binding aptamer sequence (79). The detection limit in live cells has been pushed to imaging single-molecule translation through multimerized tags, which recruit dozens of fluorescent labels (74, 113, 124, 129). The spatial resolution has also been brought into the molecular regime by the successful development of superresolution fluorescence microscopy (44).

Nevertheless, small molecules, such as cofactors, metabolites, signaling molecules, and pharmaceutical compounds, perform various biological functions. Despite their pivotal roles, unfortunately, techniques for visualizing small molecules are lagging behind those for biomacromolecules. Fluorescence microscopy has been used to visualize small molecules within single cells. For example, fluorescent analogs have been developed for lipid molecules (51); the use of fluorescent tagged antitumor drugs has led to mechanistic insights for single-cell pharmacokinetics (106). Yet fluorescence microscopy relies on labeling with fluorophores such as boron-dipyrromethene (BODIPY), rhodamines, and fluorescein dyes, which are typically larger than the small-molecule targets.

Figure 1 shows an intuitive size comparison between commonly used fluorescent tags (antibody, GFP, and organic fluorescent dye) and a typical small molecule (i.e., glucose). Because of an inevitable size mismatch, the bulky fluorescent tags often tend to alter the physicochemical properties of small-molecule targets, perturbing the intrinsic localization, interaction, and dynamics. Hence, it is challenging to adopt strategies for fluorescence imaging of biomacromolecules and apply them to small biomolecules. Consequently, the development of contrast mechanisms for small molecules primarily exploits intrinsic contrast or minimizes the size of the tag. To meet this growing demand, Raman imaging has recently emerged as a promising tool. This review focuses on quantitative mapping of small biomolecules enabled by Raman imaging. We give a general introduction first to vibrational contrast and then to both linear and nonlinear Raman imaging. Next, we present the workflow of designing small-molecule imaging. Finally, we review recent biological applications and new insights gained from small-molecule imaging (**Figure 2**).

IMAGING SMALL MOLECULES BY VIBRATIONAL CONTRAST

Although several imaging techniques have used intrinsic contrast of small molecules, including positron emission tomography (PET), magnetic resonance imaging (MRI), and mass spectrometry imaging (MSI), they often could not satisfy the required spatial resolution, detection sensitivity, molecular specificity, or live-imaging compatibility. Briefly, PET is best suited for clinical studies due to its excellent sensitivity and body penetration (4, 81). For example, the glucose analog

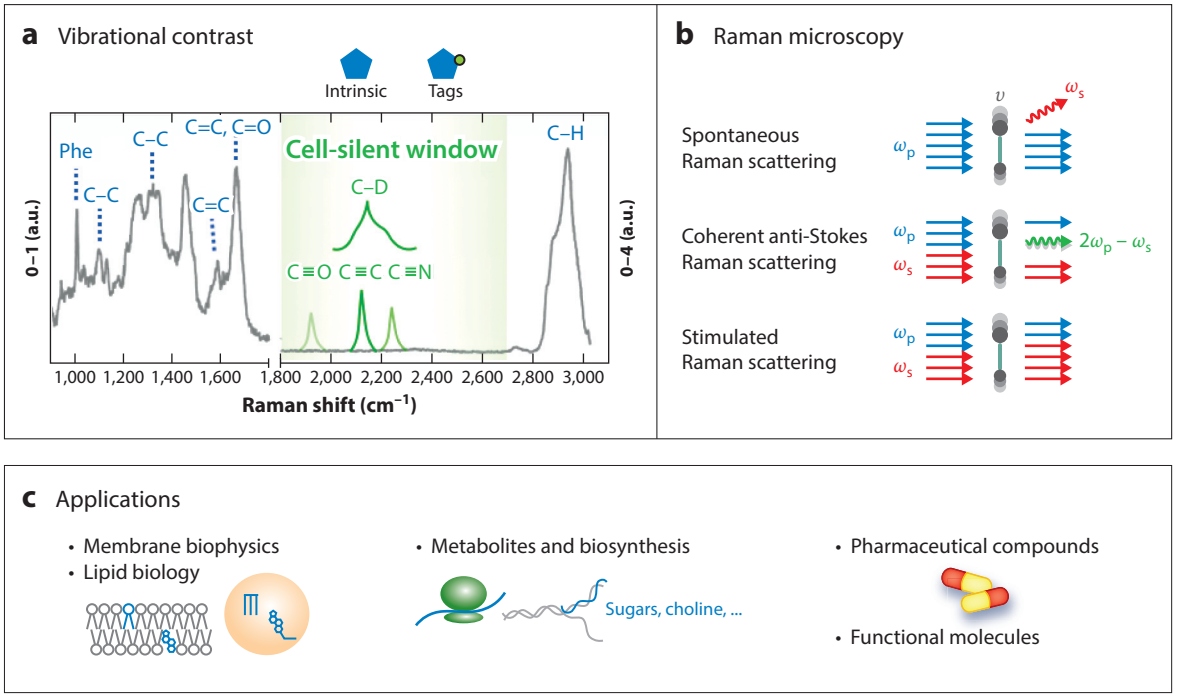

Figure 2

Principle underlying Raman imaging of small biomolecules. (*a*) Two types of vibrational contrast are explained on a Raman spectrum. Gray line shows the typical Raman spectrum of a HeLa cell from 900 cm^{-1} to 3,000 cm^{-1} wavenumber. Intrinsic contrast originates from the vibration of intrinsic chemical bonds (*blue*). Vibrational tags (*green*) show distinct Raman bands in the cell-silent window. (*b*) Three types of Raman microscopies and interactions between light and molecular vibrations. (*c*) Summary of biological applications that benefit from Raman imaging of small biomolecules. Abbreviation: Phe, phenyl group.

^{18}F-fluorodeoxyglucose (^{18}F-FDG) is frequently used to report tissue or areas with high rates of glycolysis (31, 81), and the ^{18}F-labeled anticancer drugs fluorouracil and tamoxifen have been developed to image the uptake kinetics in colorectal and breast tumors (123). However, the best-achieved spatial resolution of PET is approximately 1 mm (31), leaving out most heterogeneity occurring at the single-cell scale. Moreover, the short half-life (minute ∼ hour) of radioisotopes requires on-site synthesis of the molecular probe with expensive cyclotron and limits the interpretation of imaging results to the early steps of biochemical processes (123). Magnetic resonance spectroscopic imaging (MRSI) is another noninvasive approach that suits clinical or preclinical purposes (49). It detects the energy splitting of nuclear spin in the magnetic field, which is sensitive to the chemical environment of the nuclei, thereby generating a multivoxel spectroscopic image with high molecular specificity (33). Originally, MRSI was applied primarily to protons abundantly found in water or fat molecules, and recent technical advances in proton saturation transfer and hyperpolarization (90, 112) have improved detectability and expanded the contrast to imaging less abundant metabolites and drugs (33). Although MRSI overcomes some of the restrictions seen with PET, it is limited in sensitivity and spatial resolution, which requires 1 ∼ 100 mM molecules in a voxel dimension typically larger than 1 mm (33). Mass spectrometry (MS) has also showed potential in chemical analysis and mapping of small-molecule drugs and metabolites (64). The spatial resolution of typical imaging MS varies from 10 to 100 μm (64) and has been pushed down to 50 nm with secondary-ion MS for subcellular imaging (22, 35, 37, 47). Imaging MS is

unmatched in its molecular resolvability, yet it usually requires extensive sample preparation and desorption, which prevents its application to real-time imaging of living systems.

Recently, enhancing imaging contrast with vibrations of chemical bonds, which forms the basis of vibrational spectroscopy including infrared (IR) absorption and Raman scattering, appears promising. Because Raman scattering operates with visible or near-IR light, avoiding the strong water absorption in the IR and offering higher spatial resolution than IR microscopy, it is more popular for biological imaging. Raman scattering, first described by Raman & Krishnan (88) (the former won the 1930 Nobel Prize for Physics), refers to inelastic photon scattering by the molecule. When a molecule is illuminated, due to energy exchange between light and molecular vibration, the scattered light is at a different frequency than the incident light. The frequency difference, or Raman shift, reveals the vibrational frequency of chemical bonds in molecules. Thus, a Raman scattering spectrum, plotted as intensity against Raman shift (in cm^{-1}), contains spectral signatures from the analyte. **Figure 2*a*** shows a typical Raman spectrum from a HeLa cell, with signature bands of intrinsic chemical bonds labeled in blue. In most cases, these intrinsic chemical bonds are shared by a variety of molecules; thus, intrinsic contrast often lacks specificity. Researchers have developed a variety of vibrational tags to enhance molecular specificity (118, 143). These extrinsically introduced chemical moieties provide minimal labeling, which preserves the physicochemical properties of the molecules, while providing specific contrast in a Raman spectrum. Specifically, their vibrational peaks fall into the cell-silent window; hence, they are free from the background of intrinsic chemical bonds. Both intrinsic contrast and vibrational tags have been used for imaging small biomolecules. We review them in greater detail below.

LINEAR AND NONLINEAR RAMAN SCATTERING SPECTROSCOPY AND MICROSCOPY

When proper contrast is selected, chemical mapping of the specimen can be achieved with a Raman microscope. Three Raman imaging modalities are commonly applied (**Figure 2*b***). In spontaneous Raman scattering (93), upon interaction of molecular vibration ($\boldsymbol{v}$) and incident photon ($\boldsymbol{\omega}_p$), the scattered photon (usually with lower energy, i.e., Stokes-shifted) is spontaneously emitted at frequency $\boldsymbol{\omega}_s = \boldsymbol{\omega}_p - \boldsymbol{v}$. Technically, the specimen is illuminated by a focused monochromic continuous wave laser beam; therein, spontaneously scattered photons are collected and then dispersed by a grating to a charge-coupled device (CCD). All the Raman-active modes are excited and detected at a single shot, covering wide spectral range. Spectral resolution is determined by dispersion optics and the pixel size at the CCD, which can be as fine as $\sim 1\ cm^{-1}$. Spatial mapping is often achieved by moving the specimen and acquiring the spectra pixel by pixel. However, spontaneous Raman scattering has an intrinsically weak transition cross section ($\sigma = 10^{-28} \sim 10^{-30} cm^2$), thus requiring a long acquisition time of $1 \sim 10^2$ s per pixel, making it less ideal for fast biological imaging. Imaging speed may be improved by increasing illumination power, compromising spectral resolution, adopting line-shape illumination, or a combination thereof (77). Moreover, spontaneous Raman scattering is easily overwhelmed by the sample (auto)fluorescence, preventing image correlation to fluorescence markers.

Two other Raman imaging techniques based on coherent Raman scattering (CRS) (16), coherent anti-Stokes Raman scattering (CARS) (24, 144) and stimulated Raman scattering (SRS) (26, 76, 83) (**Figure 2*b***), have been developed to dramatically accelerate image acquisition. Both CARS and SRS are based on third-order nonlinear optical processes, requiring two synchronized picosecond or femtosecond pulsed lasers, one known as pump (ω_p) and the other Stokes (ω_s). When the energy difference ($\omega_p - \omega_s$) between pump and Stokes lasers matches with selected molecular vibration ($\boldsymbol{v}$) (i.e., on resonance), the beating field will drive the molecule to vibrate coherently and

in phase with the optical field (73). In CARS, the nonlinear polarization from each molecule generates radiation at $\omega_p + \omega_p - \omega_s$ with phase matching, which constructively interferes and produces a scattering signal at the new frequency easily separable from incident beams. Therefore, CARS is a vibration-enhanced parametric process, i.e., eventually only photon energy exchanges to produce new photons, without excitation of molecules. CARS is accompanied, however, by interfering nonresonance background, which distorts the vibrational spectra and complicates quantification.

SRS is a nonparametric process involving energy transfer from light to molecular vibration. Instead of producing a new frequency as in CARS, the generated third-order optical radiation at $\omega_s + \omega_p - \omega_s = \omega_p$ or $\omega_p - (\omega_p - \omega_s) = \omega_s$ interferes with the incident pump or Stokes beam, respectively, causing photon loss in the pump (stimulated Raman loss) and gain in the Stokes beam (stimulated Raman gain). As a result, the SRS signal is detected as intensity change in the pump or Stokes beam ($\Delta I/I = 10^{-3} \sim 10^{-7}$). A high-frequency (megahertz) modulation transfer scheme is applied to reach the shot noise detection limit by removing the low-frequency noise from slow fluctuations in laser intensity. With stimulated emission, the vibrational transition can be enhanced up to 10^8 times. Owing to linear concentration dependence, automatic phase matching, preservation of spontaneous Raman spectra, and higher detection sensitivity, SRS demonstrates a greater advantage over CARS for quantitative chemical imaging and spectral analysis.

For CRS microscopies, images are acquired by raster laser scanning at high speed ($10^{-1} \sim 10^2$ μs per pixel). The lateral resolution reaches the optical diffraction limit as in two-photon excitation, which is approximately 300 nm laterally. Spectral resolutions vary for different systems (1). In brief, shorter laser pulses produce larger signals owing to higher peak power and nonlinear power dependence, yet have broader excitation bandwidth and hence poorer spectral resolution. Regarding spectral coverage, CRS microscopy can operate in a single-frequency mode with high sensitivity and high imaging speed (91), yet only a narrow band is covered in every acquisition. Alternatively, CRS can be operated in a spectral imaging mode by a variety of techniques, which results in a hyperspectral stack of images at serial frequencies (29, 65). Hyperspectral CRS allows spectral coverage at a range of approximately 200 cm^{-1} (up to 3,000 cm^{-1}) (11) and as fast as 32 μs per pixel (62). Readers are referred to earlier reviews for tutorials on theory and technical specifications (1, 18, 61, 73, 135, 138).

WORKFLOW FOR RAMAN IMAGING OF SMALL MOLECULES

With the development of Raman microscopy, particularly the advanced SRS technique, the uniqueness and potential of Raman contrast for imaging small biomolecules have been increasingly realized. **Table 1** summarizes some recent demonstrations of small-molecule imaging. In general, the development of a targeted imaging project begins with a molecule of interest (MOI) and a question, and subsequently identifies proper vibrational contrast for the MOI and designs assays to approach the question. Here, we introduce a guideline to general readers as well as researchers interested in developing new procedures.

Selection of Raman Contrast

Some small molecules exhibit intrinsic contrasts from chemical bonds such as C=O, C=C, C–N, and C–H (**Figure 2*a***), which are the basis of label-free chemical imaging. Therefore, to start, one needs to search the Raman spectrum of the MOI for any signature peaks that are distinct from other endogenous molecules of cells or tissues. The standard solution or mixture containing the MOI should mimic the environment it encounters in cell or tissue, including pH and solvent polarity. Molecules such as porphyrin and carotenoid and their derivatives absorb at

Table 1 Raman imaging of small biomolecules and their corresponding contrasts

Molecule	Contrast		Reference(s)
Membrane biophysics			
Molecular organization of model membranes	Intrinsic, various CRS imaging	1,087 cm^{-1} (C–C, disordered) 1,128 cm^{-1} (C–C, ordered) 2,845 cm^{-1} (CH_2 polarization) I_{2880}/I_{2845} (methylene, chain order)	38, 58, 75, 89
Membrane domains	Vibrational tag, spRaman or CRS	2,100 cm^{-1} (C–D, phospholipid) 2,263 cm^{-1} (diyne, sphingomyelin)	21, 59, 85 5
Lipid unsaturation	Intrinsic, CRS	I_{1650}/I_{1450} (C=C/C–H) 3,015 cm^{-1} (C=C–H)	52, 89 57
Lipid metabolism			
Cholesterol crystal	Intrinsic, hyperspectral CRS	2,800–3,000 cm^{-1} (C–H) 1,620–1,720 cm^{-1} (C=C)	50, 65, 103 115
Sterol	Intrinsic, hyperspectral SRS	1,620–1,720 cm^{-1} (C=C) 1,745 cm^{-1} (ester C=O)	115
	Vibrational tag, spRaman or SRS	2,120 cm^{-1} (C–D) 2,254 cm^{-1} (phenyldiyne)	2, 69, 111 54
CE/TG	Intrinsic, spRaman and hyperspectral CRS	I_{702}/I_{1442} (cholesterol ring/C–H) I_{3015}/I_{2965} (C–H)	132 29
Fatty acids	Vibrational tag, spRaman or (hyperspectral) SRS	2,110 cm^{-1} (CD_2) 2,250 cm^{-1} (olefin C–D) 2,123 cm^{-1} (alkyne)	29, 69, 96, 130, 136 29, 96 15, 39, 46, 116, 119
Other metabolites			
(Deoxy)nucleotides	Vibrational tag, spRaman or SRS	2,123 [2,053] cm^{-1} (alkyne [^{13}C–])	15, 39, 41, 119, 125
Amino acids	Vibrational tag, spRaman or SRS	2,123 cm^{-1} (alkyne, Hpg) 2,133 cm^{-1} (C–D, D-amino acids) 968 cm^{-1} (phenyl ring, ^{13}C-Phe)	39, 119 110, 120, 121 95
Glucose	Vibrational tag, SRS	2,129 [2,053] cm^{-1} (alkyne [^{13}C–]) 2,120–2,133 cm^{-1} (C–D, d_7-glucose)	40, 67, 141 56, 67, 141
Mannose	Vibrational tag, SRS	2,123 cm^{-1} (alkyne)	39
Choline	Vibrational tag, SRS	2,142 cm^{-1} (alkyne) 2,188 cm^{-1} (d_9-choline)	119 42
Small-molecule drugs or inhibitors			
$[Mn(tpm)(CO)_3]Cl$	Intrinsic, spRaman	1,963 cm^{-1} (C≡O)	72
FCCP	Intrinsic, spRaman	2,176 ~ 2,230 cm^{-1} (C≡N)	127
Rhabduscin	Intrinsic, SRS	2,121 cm^{-1} (isonitrile)	19
Erlotinib	Intrinsic, spRaman	2,110 cm^{-1} (alkyne)	25
Imatinib/nilotinib	Intrinsic, hyperspectral SRS	1,305 cm^{-1} (C–C)	30
Neratinib	Intrinsic, spRaman	2,217 cm^{-1} (C≡N)	3
Fludioxonil	Intrinsic, SRS	2,219 cm^{-1} (C≡N)	114
Anisomycin	Vibrational tag, SRS	2,219 cm^{-1} (diphenylbutadiyne)	108
Ferrostatin-1	Vibrational tag, SRS	2,262 cm^{-1} (diyne)	32
Other functional molecules			
Water	Intrinsic, CARS	3,220 cm^{-1} (O–H)	84
Coenzyme Q	Vibrational tag, spRaman	2,258 cm^{-1} (phenyldiyne)	126
Acetylcholine	Intrinsic, SRS	7.20 cm^{-1} (C–N)	28
Cytochrome *c*	Intrinsic, resonance spRaman	7.50 cm^{-1} (pyrrole breathing)	36, 77

(*Continued*)

Table 1 (*Continued*)

Molecule	Contrast		Reference(s)
Carotenoid	Intrinsic, resonance spRaman	1,152∼1,158 cm^{-1} (C–C) 1,518∼1,526 cm^{-1} (C=C)	6, 10, 36, 86, 104
Retinoids	Intrinsic, hyperspectral SRS	1,605 cm^{-1} (C=C in retinol) 1,580 cm^{-1} (C=C in retinoic acid)	12, 62
Vitamin E	Intrinsic, spRaman or hyperspectral SRS	Full fingerprint spectra or 2,800 ∼ 3,000 cm^{-1} (C–H)	8, 63
Squalene	Intrinsic, hyperspectral CARS	1,665 cm^{-1} (C=C)	45

Abbreviations: CARS, coherent anti-Stokes Raman scattering; CE/TG, cholesteryl ester/triglyceride; CRS, coherent Raman scattering; FCCP, *p*-trifluoromethoxyphenylhydrazone; Hpg, L-homopropargylglycine; spRaman, spontaneous Raman scattering; SRS, stimulated Raman scattering.

approximately 450–550 nm; thus, the chromophore-associated vibrational modes would benefit from near-resonance enhancement when excited by a blue/green laser. This is particularly advantageous for spontaneous Raman imaging, which commonly implements a 532-nm laser. For example, the pyrrole breathing mode at 750 cm^{-1} in porphyrin-containing cytochrome *c* is used as a Raman marker for cell apoptosis (36, 77). Stretching of C–C (at approximately 1,154 cm^{-1}) and C=C (at approximately 1,520 cm^{-1}) bonds from the polyene chain can be used to identify carotenoid (10, 36, 86, 104). For nonabsorbing molecules such as cholesterol, signature bands such as sterol C=C can provide contrast by hyperspectral coherent Raman imaging (as will be shown in the section titled Sterol Storage and Metabolism).

Vibrational Tags of Minimal Size for Specificity and Sensitivity

The fingerprint region (600–1,800 cm^{-1}) of Raman spectra is quite crowded with endogenous chemical bonds, and the high-frequency C–H stretching region (2,800–3,200 cm^{-1}) generally lacks sufficient features. As a result, in most cases the MOI does not contain distinguishable Raman bands. Thus, vibrational tags have been recently developed to enhance imaging contrast (118, 143). They consist of only a few atoms, preserving the native function of small biomolecules; they are naturally absent inside cells and thus are biorthogonal. Vibrational tags vibrate at unique frequencies in the cell-silent window (1,800 ∼ 2,600 cm^{-1}) free of cellular background, ensuring high detection sensitivity and high specificity. Complementary to label-free vibrational imaging, this strategy has evolved into a new field of biorthogonal chemical imaging (118).

Currently, most vibrational tags fall into two major categories: stable-isotope based and triple-bond based (e.g., alkyne) (**Figure 2*a***). The heavier isotope can slow down the vibration of the associated chemical bond, thus creating new and red-shifted frequencies. For instance, C–D stretching occurs at a frequency of approximately 2,100 cm^{-1} compared with the original stretching frequency of 2,900 cm^{-1} for C–H bonds. Stable isotopes offer the minimal labeling, with essentially no alteration of the biochemical identity of the small molecule. As such, stable isotopes have been used in other analytical techniques such as nuclear magnetic resonance and quantitative mass spectroscopy. Hence, the ready availability of commercial sources could save the effort to synthesize new probes. When no commercial sources exist, customized isotopologs can also be obtained as biosynthetic product. For example, Alfonso-García et al. (2) extracted d_{38}-cholesterol from an engineered yeast strain cultured in deuterium oxide. Alternatively, bioorthogonal chemistry has introduced alkyne as a chemical handle into analogs of nucleosides, amino acids, fatty acids, glycans, and drugs to mimic their natural counterparts (34). The stretching of C≡C bonds is a strong Raman-active mode (equivalent to approximately 30 C–D bonds) and can be further enhanced by conjugation with electron-rich moiety (43, 126). In addition, the narrow linewidth of triple-bond

stretching (full width at half maximum is ~14 cm^{-1}) facilitates highly multiplexed imaging of small molecules (15, 43). Nitrile (C≡N) and carbonyl (C≡O) can also be used as Raman tags (72, 127). Notably, Yamakoshi et al. (126) conducted a systematic evaluation of a series of Raman tags for their relative Raman cross section, which could serve as a guideline for designing small-molecule Raman probes.

Optimization and Verification

Once the contrast is selected, further optimization is needed, such as time and dose if the probe is supplemented exogenously. Additional verification of function is necessary for analogs modified with vibrational tags. For example, Hu et al. (40) confirmed an alkyne-tagged glucose analog to be a good substrate of glucose transporter using glucose competition and inhibitors of transporter activity; Villareal et al. (111) applied liquid chromatography–mass spectrometry (LC-MS) to verify that the exogenously supplemented d_6-desmosterol behaved similarly to its endogenous counterpart. These verifications are necessary to ensure that Raman probes authentically report the desired process. When a new procedure is developed, applicability in different cells or tissues or even animals is assessed. Specifically, optical imaging techniques work well with monolayer cell culture, yet different cell types may differ at the endogenous level or in the incorporation efficiency of the MOI. Ex vivo tissue cultures or small animals preserve features of the multicellular organism but might introduce challenges to probe penetration or delivery and tissue light scattering.

Single-Frequency or (Hyper)spectral Imaging

The selection of a suitable Raman imaging modality also varies depending on the specific contrast. Single-frequency CRS imaging using narrow-band laser is best for targeted imaging, wherein the molecule bears an a priori–determined isolated Raman peak. For example, a 6-ps pulse corresponds to a spectral resolution of approximately 6 cm^{-1}, which is highly efficient in exciting the alkyne stretching mode (bandwidth is ~14 cm^{-1}) (119); such a scheme is called bond-selective. In cases in which the molecule's signature peaks do not fully separate from the cellular background, or several bands within a spectral range are needed to unambiguously identify the molecule, it is preferable to implement spectral imaging by spontaneous Raman microspectroscopy or hyperspectral CRS. Spectral imaging is often combined with chemometrics (2, 27, 78, 137, 142), which decomposes the overlapping spectra and recovers the underlying molecular composition. The quantitative capability of many Raman imaging techniques eventually translates image intensity into a concentration (or relative composition) map, with the guidance of a predetermined calibration curve.

From Imaging to Biological Insights

Forming a concentration map is not the end of our query. Depending on the question being asked, further biological assays are necessary for scientific interpretation. For example, subcellular localization can be inferred from the correspondence between the MOI image and known references. Raman contrast for protein (2,940 cm^{-1}) and lipid (2,845 cm^{-1}) could be used to initially evaluate possible lipophilic interactions with membrane structures. Fluorescence imaging of organelle markers is fully compatible with and can be correlated to CRS imaging in a multimodality setup, providing more precise subcellular localization. At the tissue level, marker genes can be used to identify different cell types. In some cases, image alone does not prove causation, yet offers

a valuable tool for hypothesis testing when further integrated with genetic or pharmaceutical approaches (32, 130).

BIOLOGICAL INSIGHTS FROM APPLYING RAMAN IMAGING TO MEMBRANE BIOPHYSICS AND LIPID METABOLISM

Lipids, including fatty acids, sterols, glycerolipids, and their derivatives, are essential components of the cell membrane and energy source. Though sometimes considered biomacromolecules, lipids behave more like small molecules and are fundamentally different from biopolymers such as proteins and DNA. Neutral lipids are stored in a monolayer-bound lipid droplet, which isolates them from the cytosol. Amphiphilic lipids, which contain hydrophilic heads and hydrophobic acyl chains, self-assemble into bilayers in water. This collective behavior of lipid molecules largely originates from hydrophobic interactions rather than covalent bonding (20). In this regard, Raman imaging of lipids has demonstrated great advantage over the use of fluorescence (105, 131), because the label-free or minimal labeling strategy is necessary to preserve the hydrophobicity of the lipid molecule, which underlies essentially all aspects of lipid biology. Here, we list a few examples in which Raman imaging has revealed new insights into membrane biophysics and lipid metabolism.

Membrane Lipid Organization

It has been gradually accepted that the simple fluid mosaic model (101) could not explain the preferred association between some lipids or proteins (100). The underlying principle of spontaneous phase separation has been formalized for model membrane systems, thanks to accumulating evidence from imaging studies. Characterization of phase behavior consists of preparing a model membrane by mixing several lipids with defined composition. Usually a small amount of fluorescently labeled lipid is added to the mixture. However, the fluorophore moiety inevitably alters molecular packing between the lipids (51) and thus does not necessarily report the nonfluorescent lipid species. In fact, distribution of fluorescent lipids largely reflects their own preference for different lipid phases (7).

To overcome these artifacts, researchers have applied Raman imaging based on intrinsic contrast to map molecular organization in model membrane systems. For example, the spectral difference in C–C skeletal optical modes (1,087 cm^{-1} compared with 1,128 cm^{-1}) or methylene stretching modes (2,880 cm^{-1} compared with 2,845 cm^{-1}) has been used to distinguish ordered from disordered packing (75, 89). Other contrasts, including direct quantification of molecular packing density (58) and acyl chain orientation by polarization-resolved CARS (38), have also been demonstrated. In addition to the intrinsic contrast, adoption of vibrational tags provides more chemical specificity, leading to straightforward interpretation of molecular composition. Potma & Xie (85) and Li et al. (59) showed that acyl-chain-deuterated phosphocholine allowed direct observation of domains with C–D vibration in a model membrane by CARS imaging. Recently, Donaldson & de Aguiar (21) used spontaneous Raman microscopy with chemometrics to quantify relative composition of membrane domains from a ternary mixture, in which one component is deuterated in the acyl chain. In addition, Ando et al. (5) have chemically introduced a diyne moiety at the ammonium head group of sphingomyelin. Diyne-tagged sphingomyelin showed intermolecular condensation with cholesterol comparable to that of its natural counterpart, proving good preservation of the molecular properties.

Intracellular Lipid Unsaturation

Lipid unsaturation directly contributes to its biophysical property, and thus is an informative molecular signature of intracellular lipids that are not easily measured by other techniques. To

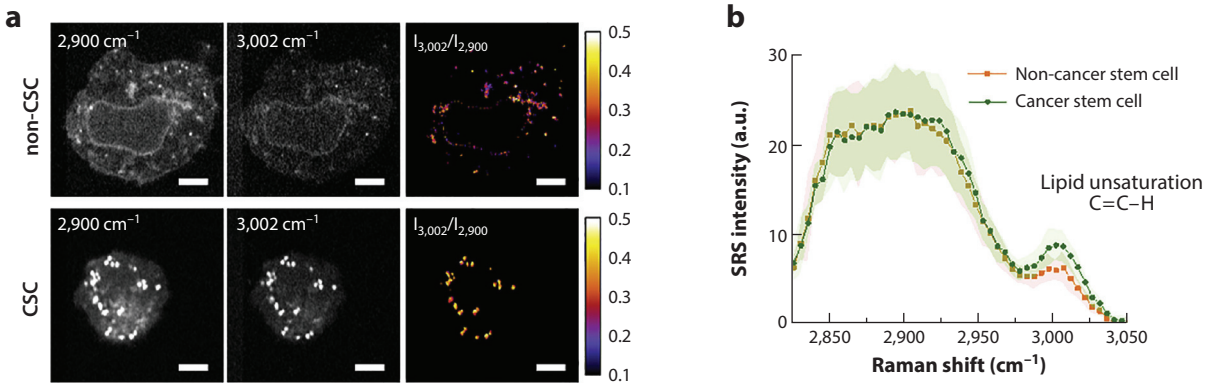

Figure 3

Raman imaging of intracellular lipid unsaturation reveals differences between non-CSCs and CSCs. (*a*) Representative hyperspectral SRS images (at 2,900 cm^{-1} and 3,002 cm^{-1}) of flow-sorted non-CSC and CSC. The intensity ratio image between the two channels quantifies lipid unsaturation. Scale bars: 10 μm. (*b*) Average SRS spectra from the lipid droplets showing higher unsaturated C–H vibration (C=C–H) at approximately 3,002 cm^{-1}. Adapted with permission from Reference 57. Abbreviations: CSC, cancer stem cell; non-CSC, non-cancer stem cell; SRS, stimulated Raman scattering.

this end, Raman imaging offers robust quantification of lipid unsaturation by targeting the intrinsic contrast from C=C bonds. For example, Rinia et al. (89) used the intensity ratio between C=C stretching and C–H bending to quantitatively image lipid unsaturation by CARS and found surprising heterogeneity in the neutral lipids stored in adipocytes. Le et al. (52) adopted a similar method to phenotype desaturase activity in *Caenorhabditis elegans*. Other Raman marker bands such as olefin C–H (3,015 cm^{-1}) were also used (29). Recently, imaging lipid unsaturation has shed light on the metabolic vulnerability of ovarian cancer. Li et al. (57) showed that cancer stem cells, a small population of persistent cancer cells responsible for tumor relapse and metastases, exhibit significantly higher lipid unsaturation than their nonstem counterparts (**Figure 3**). Higher unsaturation was also consistently found in tumor cells forming spheroids, which led the authors to examine the significance of lipid desaturase in the maintenance of cancer stemness. They then found that blocking lipid desaturase efficiently suppressed tumor initiation by cancer stem cells, rendering lipid unsaturation a valuable metabolic target of cancer therapy.

Sterol Storage and Metabolism

Sterols are a group of small lipid molecules with multiple hydrocarbon rings. Cholesterol, the major sterol found in mammals, is an essential component of mammalian cell membrane. Cholesterol concentration is critical to the membrane organization (70, 99); therefore, the free cholesterol level is closely monitored and precisely controlled by cells (87). Indeed, alteration in cholesterol storage and metabolism is associated with many diseases, including atherosclerosis and Niemann–Pick type C (70), making cholesterol a valuable disease marker and quantitative imaging of cholesterol a powerful approach to mechanistic study. Unfortunately, the available fluorescent probes for imaging cholesterol are limited. Fluorescent cholesterol analogs (e.g., dehydroergosterol) require ultraviolet excitation (71), fluorophore tagging (e.g., BODIPY-cholesterol) suffers from problems similar to those of fluorescent lipids with altered properties (71), and cholesterol binding probes (e.g., filipins) do not have enough specificity (54, 111).

Alternatively, Raman imaging is emerging as a powerful method of choice. Several studies have demonstrated CRS imaging of crystalline cholesterol (50, 65, 103), a hallmark of advanced

atherosclerotic lesions as well as primary inflammatory stimuli in the artery (23). Hyperspectral acquisition within C–H stretching (2,800–3,000 cm^{-1}) identified marker peaks in these crystals (e.g., 2,907 cm^{-1}), which confirms their chemical identity to be pure unesterified cholesterol (65, 103). Besides the use of C–H stretching, Wang et al. (115) have also visualized cholesterol crystal in intact artery tissue: Sterol C=C (1,669 cm^{-1}) can be distinguished from the acyl C=C (1,655 cm^{-1}) by hyperspectral SRS and chemometric analysis. In addition to crystalline cholesterol, Raman imaging of cholesteryl ester (CE) can be used to quantitate the intracellular cholesterol store. For example, the relative CE content in neutral lipid can be inferred from the intensity ratio between sterol C=C (1,669 cm^{-1}) and ester C=O (1,745 cm^{-1}) (115), or the ratio between olefinic C-H (3,015 cm^{-1}) and C-H (2,965 cm^{-1}) (29), or the ratio between cholesterol ring (702 cm^{-1}) and C–H bending (1,442 cm^{-1}) (132). In these studies, image quantification was calibrated by standard mixture containing CE and triglyceride, offering in situ chemical analysis of lipid storage. Notably, these efforts have offered important mechanistic insights. For example, Yue et al. (132) performed quantitative analysis on prostate cancer clinical samples, cell lines, and mouse tumor xenograft models and found aberrant accumulation of CE in the lipid droplet of high-grade prostate cancer and metastases. Through genetic and pharmaceutical manipulation, they revealed that CE accumulation was caused by loss of the tumor suppressor PTEN and subsequent activation of the PI3K/AKT pathway, which increases cholesterol uptake through lipoprotein. Importantly, abrogating cholesterol esterification by small-molecule inhibitors reduced cancer cell aggressiveness and impaired tumor growth in mouse xenografts, offering a new therapeutic approach by targeting increased cholesterol demand in tumor cells.

Although the above intrinsic Raman bands enable identification of cholesterol in crystal or lipid droplets, they are still mixed with other cellular bands, making it difficult to specifically image cholesterol in other complex cellular environments. In addition, they are not suited for studying the dynamics. Thus, several studies have introduced vibrational tags for imaging cholesterol and its trafficking. Matthäus et al. (69) used commercially available d_6–2,2,3,4,4,6-cholesterol to image the dynamics of uncontrolled cholesterol uptake and accumulation in monocyte-derived macrophages. To enhance signal, Alfonso-García et al. (2) extracted d_{38}-cholesterol from D_2O-cultured yeast engineered to produce cholesterol instead of ergosterol. Hyperspectral analysis revealed that the intracellular lipid droplets vary in their rate of cholesterol incorporation as well as CE level. Lee et al. (54) synthesized a series of alkyne-tagged cholesterol analogs, among which phenyl-diyne cholesterol (PhDY-chol) produces the largest signal and minor cytotoxicity. Using PhDY-chol allowed the authors to visualize membrane distribution as well as drug-induced cholesterol mobilization from lysosome to lipid droplets in a cellular model of Niemann–Pick type C disease. By feeding *C. elegans* with PhDY-chol, they also found that cholesterol was stored in lysosome-related organelles rather than lipid droplets in intestine. Beyond cholesterol, Villareal et al. (111) have investigated the localization of desmosterols during hepatitis C virus (HCV) infection, a major cause of liver cancer and fatty liver diseases. Using SRS imaging, the authors found trafficking and accumulation of deuterated desmosterol in lipid droplets closely associated with HCV core protein, implying a mechanistically important role for desmosterol in viral replication. By imaging structurally similar sterols, they confirmed that the action of HCV is very specific to desmosterol, demonstrating characterization of molecular structure while resolving the intracellular localization.

Fatty Acid Metabolism and Lipotoxicity

Fatty acids include a diverse collection of molecular structures with varying chain length (m) and number of unsaturated bonds (n), often denoted as Cm:n. Even a minute difference in structure

could result in completely different biophysical and biochemical properties. Traditionally, mass spectrometry is utilized to cover such diversity and distinguish the structurally similar components, which leads to a comprehensive approach called lipidomics (122). Yet when it comes to trafficking of a specific type of fatty acid, Raman imaging of labeled fatty acid has demonstrated great advantage and has elucidated lipid biology.

Both deuterated and alkyne-tagged fatty acids have been used as Raman probes. For example, using deuterated palmitate (C16:0) or oleate (C18:1), several groups have demonstrated Raman imaging of fatty acid incorporation into lipid droplets, where they are stored as triglyceride or CE (29, 69, 102, 116, 130, 136). Notably, Fu et al. (29) further exploited the spectral difference between fully deuterated palmitate (CD_2 symmetric stretch) and d_8-arachidonic acid (C20:4, olefin C–D) to simultaneously track these two fatty acids in *C. elegans*. Shen et al. (96) have followed this strategy to reveal differential intracellular trafficking of palmitate and oleate. Alternatively, alkyne-tagged palmitic acid, 17-octadecynoic acid, can also be used to report lipid droplet or membrane incorporation (15, 39, 116, 119). Alkyne tagging inadvertently changes, albeit slightly, the property of fatty acid, yet the narrow bandwidth of alkyne ($\sim$15 cm^{-1}) makes multiplexing easier than does broadband C–D stretching ($\sim$100 cm^{-1}) (15).

The ability to authentically report fatty acid trafficking provides exciting opportunity for understanding lipid biology and disease mechanisms. One particular motif is the wide appearance of metabolic disorders associated with a modern lifestyle and overnutrition, such as diabetes and obesity. Under these pathological conditions, an elevated level of fatty acids in the bloodstream is believed to cause cell death and tissue dysfunction, collectively termed lipotoxicity (94, 109). However, despite extensive biochemical research (53, 94), it remained unclear how fatty acids, especially saturated ones, disturb cell homeostasis. Utilizing SRS imaging of deuterated fatty acids, Shen et al. (96) recently provided new insights into lipotoxicity, linking fatty acid metabolism to endoplasmic reticulum membrane biophysics. A remarkable difference was observed between the deuterated fatty acid probe and its fluorescent analog (**Figure 4*a***). A clear phase separation pattern between the two probes (**Figure 4*b***) led the authors to examine the physical property of palmitate metabolites, which was determined to be in solid phase. This marked the first time that solid-phase membrane was observed in living mammalian cells. By establishing a correlation to fluorescent organelle markers, the authors found that palmitate-derived solid membrane domains localize to endoplasmic reticulum, which is presumably fluidic in physiological condition (**Figure 4*c***). Interestingly, unsaturated fatty acids do not lead to solid domain formation. Among several saturated fatty acids tested, the longer chain leads to a more solid membrane. Together, this finding is well correlated with the cytotoxicity of the different fatty acids, suggesting a causative role for solid membrane in lipotoxicity.

IMAGING METABOLITES FOR BIOSYNTHETIC ACTIVITY

In addition to tracking lipids, Raman imaging has been used to track other metabolites, including (deoxy)nucleotides, amino acids, and sugars, mostly with the biorthogonal chemical imaging strategy using vibrational tags. For example, alkyne-tagged deoxyribonucleoside ethynyl-deoxyuridine has been used to report DNA synthesis and therefore cell proliferation in cultured cells (15, 39, 119, 125) as well as in *C. elegans* (119) and tissue slices (41). Alkyne-tagged ribonucleoside ethynyluridine has been used to quantify RNA turnover (119). The alkyne-tagged methionine analog L-homopropargylglycine (Hpg) was imaged to visualize protein synthesis (39, 119). Similarly, using a genetically encodable unnatural amino acid, Zhang et al. (140) were able to label a specific protein with Raman tag and observe the protein's intracellular localization. Owing to the low incorporation rate of modified amino acid (9), isotope-labeled amino acids are preferred for optimal

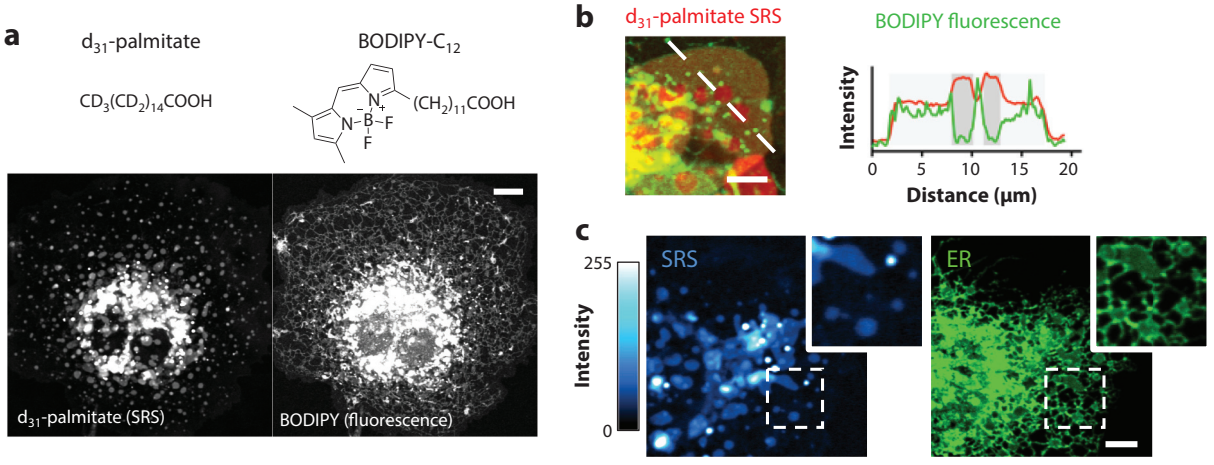

Figure 4

Application of Raman imaging to fatty acid metabolism and lipotoxicity. (*a*) Two probes for saturated fatty acid, including a Raman probe, d_{31}-palmitate, and a fluorescent probe, BODIPY-C_{12}, were used to report lipid synthesis in the same COS-7 cell. They revealed remarkably different spatial distribution patterns. Scale bar: 10 μm. (*b*) Similar to panel *a*, SRS image (*red*) and BODIPY fluorescence image (*green*) were overlaid at an area of intracellular membrane. Intensity profiles across the dashed line show negative correlation between the two channels, indicating phase separation in the membrane lipids. Scale bar: 2 μm. (*c*) Correlative imaging of a fluorescent ER marker, ER-GFP, helps identify subcellular compartments for d_{31}-palmitate-derived membrane. Scale bar: 5 μm. Adapted with permission from Reference 96. Abbreviations: BODIPY, boron-dipyrromethene; ER-GFP, endoplasmic reticulum–green fluorescent protein; SRS, stimulated Raman scattering.

incorporation and labeling efficiency. For example, the C–D stretching mode in d_5-phenylalanine and the ring breathing mode of U-^{13}C-phenylalanine can be used as quantitative reporters of protein synthesis and turnover dynamics (95, 110). A mixture of deuterated amino acids further boosts the signal (121), which makes measuring protein synthesis feasible even in small animals (97, 120).

Raman probes for sugars have also been developed. Hu et al. (40) synthesized an alkyne-tagged glucose (3-OPG) to report short-term glucose-uptake activity in normal and cancerous cells. d_7-Glucose is used to detect de novo lipogenesis in lipid droplets or membranes when targeting at the C–D vibration enriched in lipids (56, 67, 141). Interestingly, the ratio between these two activities, which represents the efficiency of glucose converted into biomass, is an important marker that distinguishes normal from cancerous cells due to the Warburg effect (14). To this end, Long et al. (67) synthesized ^{13}C-alkyne-tagged glucose so that the originally overlapping alkyne and C–D peaks could be fully resolved for two-color imaging of glucose utilization. In addition to the use of glucose as a probe, an alkyne-tagged mannose analog is a suitable metabolic probe for imaging glycan (39). Last, alkyne-tagged and d_9-labeled choline have been used to report membrane lipid synthesis (42, 119). Most of these metabolic imaging efforts benefit from the high enrichment in macromolecules (concentration around mM) rather than the free pool (μM) of the metabolite (82), which essentially report specific biosynthetic activity toward metabolic assessment at the single-cell level (134). For a more detailed review, readers are referred to References 118 and 143.

IMAGING SMALL-MOLECULE DRUGS AND OTHER FUNCTIONAL MOLECULES

Small-molecule drugs are another family of small biomolecules with crucial functions. Visualization of the uptake, localization, and metabolism of small-molecule drugs in living systems can

greatly facilitate the study of molecular regulation in biological systems and accelerate the early stages of the drug discovery process. Noninvasive molecular imaging techniques such as positron emission tomography, fluorescence, and Raman microscopy have been developed and applied to visualize small-molecule drugs (123). Among these, Raman microscopy together with vibrational tags becomes a promising tool for high-resolution imaging of small-molecule drugs (107), thanks to maximal preservation of functional activity, subcellular localization, and intracellular interaction.

Raman imaging of drugs has been achieved with alkyne, nitrile, and carbonyl moieties. With spontaneous Raman microscopy, Meister et al. (72) imaged an antitumor manganese metal-carbonyl complex in live cancer cells using the strong C≡O vibrations as intrinsic labels. Yamakoshi et al. (127) used intrinsic nitriles as structure-sensitive Raman tags to image both protonated and deprotonated forms of the mitochondrial uncoupler *p*-trifluoromethoxyphenylhydrazone in live cells by spontaneous Raman microscopy. SRS provides more sensitive imaging of small-molecule drugs. Rhabduscin, a natural product produced by gram-negative pathogens, was imaged by SRS microscopy with the intrinsic isonitrile group. Intense localization of rhabduscin was observed in the cell periphery of bacteria (19). Depth-resolved SRS imaging of the delivery of a skin drug, terbinafine, was achieved in mouse ear tissue by targeting at the alkyne vibration in the molecule. The drug penetrated through the lipid-rich structures, consistent with its lipophilic properties (119). SRS imaging has also revealed distribution of the fungicide fludioxonil in the seed coat based on its intrinsic C≡N bond (114).

Raman imaging has uncovered the intracellular pharmacokinetics of tyrosine kinase inhibitors, an important class of FDA-approved drugs for anticancer treatment. For example, erlotinib and neratinib, two epidermal growth factor receptor inhibitors, naturally bear an alkyne tag and a nitrile tag, respectively (3, 25). They cluster at the cell surface or inside lysosomes, respectively. Moreover, metabolic products of neratinib were identified by hyperspectral analysis, density functional theory calculations, and LC-MS, demonstrating the potential of Raman imaging to study the pharmacokinetics of drugs in cells. Two other tyrosine kinase inhibitors, imatinib and nilotinib, were visualized by hyperspectral SRS imaging based on C–C stretching (30). By staining with fluorescent lysosome marker, they were found significantly enriched inside lysosomes (**Figure 5*a***). Co-treatment with chloroquine reduced the lysosome trapping of imatinib, which might increase the efficacy of imatinib through lysosome-mediated drug–drug interaction.

For drugs without inherently strong and characteristic vibrational moieties, their visualization can be achieved by selectively attaching with Raman tags for enhanced sensitivity and specificity. Yamakoshi et al. (126) synthesized and visualized small-molecule coenzyme Q analogs in the mitochondria of live cells using diyne-tag Raman imaging. Anisomycin, a potent protein synthesis inhibitor, was visualized in live cells by attaching it to an intense diphenylbutadiyne Raman tag and its uptake kinetics was monitored with time-lapse SRS microscopy (108). Gaschler et al. (32) reported SRS imaging of intracellular distribution of a ferroptosis inhibitor, ferrostatin-1, in live cells by installing a small diyne tag (**Figure 5*b***). After confirming the preservation of drug efficacy, the authors found that accumulation of ferrostatin-1 in mitochondria and lysosomes did not contribute to ferroptosis suppression, suggesting endoplasmic reticulum is a likely key membrane-rich organelle involved in ferroptosis (32).

Many other functional biomolecules are also interesting targets of Raman imaging. Potma et al. (84) applied a CARS microscope to visualize H_2O/D_2O exchange in real time, which reveals transient intracellular hydrodynamics. Severely restricted water motion was found near the plasma membrane of a microorganism (84). Fu et al. (28) applied hyperspectral SRS to image acetylcholine, an important neurotransmitter that relays neural excitation from lower motor neurons to muscles. Using the intrinsic contrast of acetylcholine, they achieved quantitative imaging in the

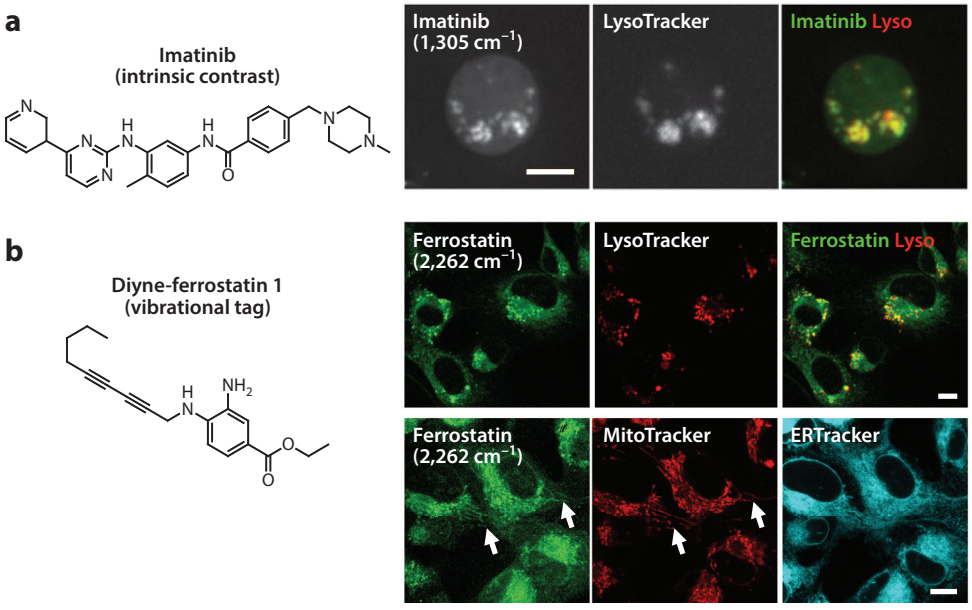

Figure 5

Raman imaging of small-molecule drugs. (*a*) Structure of imatinib (*far left*) and its distribution in a BaF3/BCR-ABL1 cell (*left*). SRS image was acquired at 1,305 cm^{-1} after treatment with 20 μM imatinib. Merged image (*right*) shows overlap between the SRS image (*left*) and a fluorescent lysosome marker, LysoTracker Red (*center*). Adapted with permission from Reference 30. Scale bar: 5 μm. (*b*) Structure of diyne-ferrostatin 1 (*far left*) and its localization in live HT-1080 cells (treated with erastin) (*left*). SRS images obtained at 2,262 cm^{-1} (diyne) (*left*, *top and bottom*) were compared with fluorescent images of organelle markers, including LysoTracker Red (lysosome) (*center*, *top*), MitoTracker Deep Red (mitochondria) (*center*, *bottom*), and ERTracker Green (*right*, *bottom*). Arrows indicate the localization of ferrostatin to mitochondria. Scale bars: 10 μm. Adapted with permission from Reference 32. Abbreviations: ER, endoplasmic reticulum; SRS, stimulated Raman scattering.

neuromuscular junction of frog muscle, where the local concentration is approximately 10 mM. Raman imaging has also been successfully applied to map the biodistribution of antioxidants, including carotenoids (6, 10, 36, 86, 104), retinoids (12, 62), and vitamin E (8, 63), as well as the distribution of the biofuel squalene in algae (45), revealing their crucial roles in metabolic homeostasis.

FUTURE PERSPECTIVES

Innovation of chemical imaging techniques is bringing more molecules under the illumination of modern light microscopy (17). In terms of contrast, intrinsic vibrational signatures for more small molecules will continue to be examined, while designing and synthesizing novel Raman probes will provide opportunities for other target molecules. The remaining challenge for Raman imaging is detection of low-abundance molecules (less than tens of micromolar in local concentration), which calls for next-generation vibrational tags with enhanced sensitivity. In addition to direct detection, chemical specificity can also be achieved with molecular sensors that undergo Raman spectral change upon binding to a MOI (127, 133). Moreover, adding functional moiety for subcellular targeting makes a variety of organelle molecular probes (43, 60, 128). The information content can be scaled up by simultaneous imaging of multiple small biomolecules,

which was first achieved with an isotope-edited alkyne tag (15). Recent efforts from our group have expanded the color palette of vibrational tags and achieved supermultiplex imaging (up to 24 colors) (43, 117), which revealed the possibility of single-cell spectroscopic profiling. Instrument-wise, the vast interest in seeing molecules in live animals could be fulfilled by the development of a new CRS endoscope (66, 92); further improvement in spatial resolution beyond the optical diffraction limit has also been proposed and implemented for imaging material (48, 98, 139), and will hopefully be implemented for small molecules in the near future. Though this review focuses on Raman imaging and its advantages, one should be constantly reminded that comprehensive knowledge of a biological process requires integrated analysis by multiple techniques. Therefore, it is also worthwhile to combine or correlate Raman imaging with other imaging modalities, such as ultrastructural imaging by electron microscopy or chemically informative MSI (68).

DISCLOSURE STATEMENT

The authors are not aware of any affiliations, memberships, funding, or financial holdings that might be perceived as affecting the objectivity of this review.

ACKNOWLEDGMENTS

The authors appreciate contributions from all previous and current members of the Min group. W.M. acknowledges support from a National Institutes of Health Director's New Innovator Award, NIH R01 (grant EB020892), the Alfred P. Sloan Foundation, the Camille and Henry Dreyfus Foundation, and a Pilot and Feasibility grant from the New York Obesity Nutrition Research Center. Y.S. acknowledges support from a Howard Hughes Medical Institute International Student Research Fellowship. F.H. acknowledges support from a Raymond and Beverly Sackler Center Postdoctoral Fellowship.

LITERATURE CITED

1. Alfonso-García A, Mittal R, Lee ES, Potma EO. 2014. Biological imaging with coherent Raman scattering microscopy: a tutorial. *J. Biomed. Opt.* 19(7):71407
2. Alfonso-García A, Pfisterer SG, Riezman H, Ikonen E, Potma EO. 2016. D38-cholesterol as a Raman active probe for imaging intracellular cholesterol storage. *J. Biomed. Opt.* 21(6):61003
3. Aljakouch K, Lechtonen T, Yosef HK, Hammoud MK, Alsaidi W, et al. 2018. Raman microspectroscopic evidence for the metabolism of a tyrosine kinase inhibitor, neratinib, in cancer cells. *Angew. Chem. Int. Ed.* 57(24):7250–54
4. Ametamey SM, Honer M, Schubiger PA. 2008. Molecular imaging with PET. *Chem. Rev.* 108(5):1501–16
5. Ando J, Kinoshita M, Cui J, Yamakoshi H, Dodo K, et al. 2015. Sphingomyelin distribution in lipid rafts of artificial monolayer membranes visualized by Raman microscopy. *PNAS* 112(15):4558–63
6. Ashtikar M, Matthäus C, Schmitt M, Krafft C, Fahr A, Popp J. 2013. Non-invasive depth profile imaging of the stratum corneum using confocal Raman microscopy: first insights into the method. *Eur. J. Pharm. Sci.* 50(5):601–8
7. Baumgart T, Hunt G, Farkas ER, Webb WW, Feigenson GW. 2007. Fluorescence probe partitioning between L_o/L_d phases in lipid membranes. *Biochim. Biophys. Acta* 1768(9):2182–94
8. Beattie JR, Maguire C, Gilchrist S, Barrett LJ, Cross CE, et al. 2007. The use of Raman microscopy to determine and localize vitamin E in biological samples. *FASEB J.* 21(3):766–76

9. Beatty KE, Liu JC, Xie F, Dieterich DC, Schuman EM, et al. 2006. Fluorescence visualization of newly synthesized proteins in mammalian cells. *Angew. Chem. Int. Ed.* 45(44):7364–67
10. Brozek-Pluska B, Musial J, Kordek R, Bailo E, Dieing T, Abramczyk H. 2012. Raman spectroscopy and imaging: applications in human breast cancer diagnosis. *Analyst* 137(16):3773–80
11. Camp CH, Lee YJ, Heddleston JM, Hartshorn CM, Walker ARH, et al. 2014. High-speed coherent Raman fingerprint imaging of biological tissues. *Nat. Photon.* 8(8):627–34
12. Chen AJ, Li J, Jannasch A, Mutlu AS, Wang MC, Cheng J-X. 2018. Fingerprint stimulated Raman scattering imaging reveals retinoid coupling lipid metabolism and survival. *Chemphyschem* 19(19):2500–6
13. Chen B, Gilbert LA, Cimini BA, Schnitzbauer J, Zhang W, et al. 2013. Dynamic imaging of genomic loci in living human cells by an optimized CRISPR/Cas system. *Cell* 155(7):1479–91
14. Chen YJ, Huang X, Mahieu NG, Cho K, Schaefer J, Patti GJ. 2014. Differential incorporation of glucose into biomass during Warburg metabolism. *Biochemistry* 53(29):4755–57
15. Chen Z, Paley DW, Wei L, Weisman AL, Friesner RA, et al. 2014. Multicolor live-cell chemical imaging by isotopically edited alkyne vibrational palette. *J. Am. Chem. Soc.* 136(22):8027–33
16. Cheng J-X, Xie XS. 2013. *Coherent Raman Scattering Microscopy*. Boca Raton, FL: CRC Press
17. Cheng J-X, Xie XS. 2015. Vibrational spectroscopic imaging of living systems: an emerging platform for biology and medicine. *Science* 350(6264):aaa8870
18. Chung C-Y, Potma EO. 2013. Biomolecular imaging with coherent nonlinear vibrational microscopy. *Annu. Rev. Phys. Chem.* 64:77–99
19. Crawford JM, Portmann C, Zhang X, Roeffaers MBJ, Clardy J. 2012. Small molecule perimeter defense in entomopathogenic bacteria. *PNAS* 109(27):10821–26
20. Cullis PR, Fenske DB, Hope MJ. 2008. Physical properties and functional roles of lipids in membranes. In *Biochemistry of Lipids, Lipoproteins and Membranes*, ed. DE Vance, JE Vance, pp. 1–37. Elsevier. 5th ed.
21. Donaldson SH, de Aguiar HB. 2018. Molecular imaging of cholesterol and lipid distributions in model membranes. *J. Phys. Chem. Lett.* 9(7):1528–33
22. Drozdz MM, Jiang H, Pytowski L, Grovenor C, Vaux DJ. 2017. Formation of a nucleoplasmic reticulum requires de novo assembly of nascent phospholipids and shows preferential incorporation of nascent lamins. *Sci. Rep.* 7(1):7454
23. Duewell P, Kono H, Rayner KJ, Sirois CM, Vladimer G, et al. 2010. NLRP3 inflammasomes are required for atherogenesis and activated by cholesterol crystals. *Nature* 464(7293):1357–61
24. Duncan MD, Reintjes J, Manuccia TJ. 1982. Scanning coherent anti-Stokes Raman microscope. *Opt. Lett.* 7(8):350–52
25. El-Mashtoly SF, Petersen D, Yosef HK, Mosig A, Reinacher-Schick A, et al. 2014. Label-free imaging of drug distribution and metabolism in colon cancer cells by Raman microscopy. *Analyst* 139(5):1155–61
26. Freudiger CW, Min W, Saar BG, Lu S, Holtom GR, et al. 2008. Label-free biomedical imaging with high sensitivity by stimulated Raman scattering microscopy. *Science* 322(5909):1857–61
27. Fu D, Xie XS. 2014. Reliable cell segmentation based on spectral phasor analysis of hyperspectral stimulated Raman scattering imaging data. *Anal. Chem.* 86(9):4115–19
28. Fu D, Yang W, Xie XS. 2017. Label-free imaging of neurotransmitter acetylcholine at neuromuscular junctions with stimulated Raman scattering. *J. Am. Chem. Soc.* 139(2):583–86
29. Fu D, Yu Y, Folick A, Currie E, Farese RV Jr., et al. 2014. In vivo metabolic fingerprinting of neutral lipids with hyperspectral stimulated Raman scattering microscopy. *J. Am. Chem. Soc.* 136(24):8820–28
30. Fu D, Zhou J, Zhu WS, Manley PW, Wang YK, et al. 2014. Imaging the intracellular distribution of tyrosine kinase inhibitors in living cells with quantitative hyperspectral stimulated Raman scattering. *Nat. Chem.* 6(7):614–22
31. Gambhir SS. 2002. Molecular imaging of cancer with positron emission tomography. *Nat. Rev. Cancer* 2(9):683–93
32. Gaschler MM, Hu F, Feng H, Linkermann A, Min W, Stockwell BR. 2018. Determination of the subcellular localization and mechanism of action of ferrostatins in suppressing ferroptosis. *ACS Chem. Biol.* 13(4):1013–20

33. Glunde K, Artemov D, Penet M-F, Jacobs MA, Bhujwalla ZM. 2010. Magnetic resonance spectroscopy in metabolic and molecular imaging and diagnosis of cancer. *Chem. Rev.* 110(5):3043–59
34. Grammel M, Hang HC. 2013. Chemical reporters for biological discovery. *Nat. Chem. Biol.* 9(8):475–84
35. Guillermier C, Poczatek JC, Taylor WR, Steinhauser ML. 2017. Quantitative imaging of deuterated metabolic tracers in biological tissues with nanoscale secondary ion mass spectrometry. *Int. J. Mass Spectrom.* 422:42–50
36. Hashimoto A, Yamaguchi Y, Chiu L-d, Morimoto C, Fujita K, et al. 2015. Time-lapse Raman imaging of osteoblast differentiation. *Sci. Rep.* 5:12529
37. He C, Weston TA, Jung RS, Heizer P, Larsson M, et al. 2018. NanoSIMS analysis of intravascular lipolysis and lipid movement across capillaries and into cardiomyocytes. *Cell Metab.* 27(5):1055–66.e3
38. Hofer M, Balla NK, Brasselet S. 2017. High-speed polarization-resolved coherent Raman scattering imaging. *Optica* 4(7):795–801
39. Hong S, Chen T, Zhu Y, Li A, Huang Y, Chen X. 2014. Live-cell stimulated Raman scattering imaging of alkyne-tagged biomolecules. *Angew. Chem. Int. Ed.* 53(23):5827–31
40. Hu F, Chen Z, Zhang L, Shen Y, Wei L, Min W. 2015. Vibrational imaging of glucose uptake activity in live cells and tissues by stimulated Raman scattering. *Angew. Chem. Int. Ed.* 54(34):9821–25
41. Hu F, Lamprecht MR, Wei L, Morrison B, Min W. 2016. Bioorthogonal chemical imaging of metabolic activities in live mammalian hippocampal tissues with stimulated Raman scattering. *Sci. Rep.* 6(1):39660
42. Hu F, Wei L, Zheng C, Shen Y, Min W. 2014. Live-cell vibrational imaging of choline metabolites by stimulated Raman scattering coupled with isotope-based metabolic labeling. *Analyst* 139(10):2312–17
43. Hu F, Zeng C, Long R, Miao Y, Wei L, et al. 2018. Supermultiplexed optical imaging and barcoding with engineered polyynes. *Nat. Methods* 15(3):194–200
44. Huang B, Bates M, Zhuang X. 2009. Super-resolution fluorescence microscopy. *Annu. Rev. Biochem.* 78:993–1016
45. Ishitsuka K, Koide M, Yoshida M, Segawa H, Leproux P, et al. 2017. Identification of intracellular squalene in living algae, *Aurantiochytrium mangrovei* with hyper-spectral coherent anti-Stokes Raman microscopy using a sub-nanosecond supercontinuum laser source. *J. Raman Spectrosc.* 48:8–15
46. Jamieson LE, Greaves J, McLellan JA, Munro KR, Tomkinson NCO, et al. 2018. Tracking intracellular uptake and localisation of alkyne tagged fatty acids using Raman spectroscopy. *Spectrochim. Acta A Mol. Biomol. Spectrosc.* 197:30–36
47. Jiang H, Goulbourne CN, Tatar A, Turlo K, Wu D, et al. 2014. High-resolution imaging of dietary lipids in cells and tissues by NanoSIMS analysis. *J. Lipid Res.* 55(10):2156–66
48. Kim H, Bryant GW, Stranick SJ. 2012. Superresolution four-wave mixing microscopy. *Opt. Express* 20(6):6042–51
49. Kim MM, Parolia A, Dunphy MP, Venneti S. 2016. Non-invasive metabolic imaging of brain tumours in the era of precision medicine. *Nat. Rev. Clin. Oncol.* 13(12):725–39
50. Kim SH, Lee ES, Lee JY, Lee ES, Lee BS, et al. 2010. Multiplex coherent anti-Stokes Raman spectroscopy images intact atheromatous lesions and concomitantly identifies distinct chemical profiles of atherosclerotic lipids. *Circ. Res.* 106(8):1332–41
51. Klymchenko AS, Kreder R. 2014. Fluorescent probes for lipid rafts: from model membranes to living cells. *Chem. Biol.* 21(1):97–113
52. Le TT, Duren HM, Slipchenko MN, Hu CD, Cheng JX. 2010. Label-free quantitative analysis of lipid metabolism in living *Caenorhabditis elegans*. *J. Lipid Res.* 51(3):672–77
53. Leamy AK, Egnatchik RA, Young JD. 2013. Molecular mechanisms and the role of saturated fatty acids in the progression of non-alcoholic fatty liver disease. *Prog. Lipid Res.* 52(1):165–74
54. Lee HJ, Zhang W, Zhang D, Yang Y, Liu B, et al. 2015. Assessing cholesterol storage in live cells and *C. elegans* by stimulated Raman scattering imaging of phenyl-diyne cholesterol. *Sci. Rep.* 5:7930
55. Levsky JM, Singer RH. 2003. Fluorescence in situ hybridization: past, present and future. *J. Cell Sci.* 116(14):2833–38
56. Li J, Cheng J-X. 2015. Direct visualization of de novo lipogenesis in single living cells. *Sci. Rep.* 4(1):6807
57. Li J, Condello S, Thomes-Pepin J, Ma X, Xia Y, et al. 2017. Lipid desaturation is a metabolic marker and therapeutic target of ovarian cancer stem cells. *Cell Stem Cell* 20(3):303–14.e5

58. Li L, Cheng JX. 2008. Label-free coherent anti-Stokes Raman scattering imaging of coexisting lipid domains in single bilayers. *J. Phys. Chem. B* 112(6):1576–79
59. Li L, Wang H, Cheng J-X. 2005. Quantitative coherent anti-Stokes Raman scattering imaging of lipid distribution in coexisting domains. *Biophys. J.* 89(5):3480–90
60. Li X, Jiang M, Lam JWY, Tang BZ, Qu JY. 2017. Mitochondrial imaging with combined fluorescence and stimulated Raman scattering microscopy using a probe of the aggregation-induced emission characteristic. *J. Am. Chem. Soc.* 139(47):17022–30
61. Liao C-S, Cheng J-X. 2016. In situ and in vivo molecular analysis by coherent Raman scattering microscopy. *Annu. Rev. Anal. Chem.* 9:69–93
62. Liao C-S, Slipchenko MN, Wang P, Li J, Lee S-Y, et al. 2015. Microsecond scale vibrational spectroscopic imaging by multiplex stimulated Raman scattering microscopy. *Light Sci. Appl.* 4:e265
63. Liao CS, Wang P, Wang P, Li J, Lee HJ, et al. 2015. Spectrometer-free vibrational imaging by retrieving stimulated Raman signal from highly scattered photons. *Sci. Adv.* 1(9):e1500738
64. Lietz CB, Gemperline E, Li L. 2013. Qualitative and quantitative mass spectrometry imaging of drugs and metabolites. *Adv. Drug Deliv. Rev.* 65(8):1074–85
65. Lim RS, Suhalim JL, Miyazaki-Anzai S, Miyazaki M, Levi M, et al. 2011. Identification of cholesterol crystals in plaques of atherosclerotic mice using hyperspectral CARS imaging. *J. Lipid Res.* 52(12):2177–86
66. Lombardini A, Mytskaniuk V, Sivankutty S, Andresen ER, Chen X, et al. 2018. High-resolution multimodal flexible coherent Raman endoscope. *Light Sci. Appl.* 7:10
67. Long R, Zhang L, Shi L, Shen Y, Hu F, et al. 2018. Two-color vibrational imaging of glucose metabolism by stimulated Raman scattering. *Chem. Commun.* 54(2):152–55
68. Marty F, Rago G, Smith DF, Gao X, Eijkel GB, et al. 2017. Combining time-of-flight secondary ion mass spectrometry imaging mass spectrometry and CARS microspectroscopy reveals lipid patterns reminiscent of gene expression patterns in the wing imaginal disc of *Drosophila melanogaster*. *Anal. Chem.* 89(18):9664–70
69. Matthäus C, Krafft C, Dietzek B, Brehm BR, Lorkowski S, Popp J. 2012. Noninvasive imaging of intracellular lipid metabolism in macrophages by Raman microscopy in combination with stable isotopic labeling. *Anal. Chem.* 84(20):8549–56
70. Maxfield FR, Tabas I. 2005. Role of cholesterol and lipid organization in disease. *Nature* 438(7068):612–21
71. Maxfield FR, Wüstner D. 2012. Analysis of cholesterol trafficking with fluorescent probes. *Methods Cell Biol.* 108:367–93
72. Meister K, Niesel J, Schatzschneider U, Metzler-Nolte N, Schmidt DA, Havenith M. 2010. Label-free imaging of metal-carbonyl complexes in live cells by Raman microspectroscopy. *Angew. Chem. Int. Ed.* 49(19):3310–12
73. Min W, Freudiger CW, Lu S, Xie XS. 2011. Coherent nonlinear optical imaging: beyond fluorescence microscopy. *Annu. Rev. Phys. Chem.* 62:507–30
74. Morisaki T, Lyon K, DeLuca KF, DeLuca JG, English BP, et al. 2016. Real-time quantification of single RNA translation dynamics in living cells. *Science* 352(6292):1425–29
75. Müller M, Schins JM. 2002. Imaging the thermodynamic state of lipid membranes with multiplex CARS microscopy. *J. Phys. Chem. B* 106(14):3715–23
76. Nandakumar P, Kovalev A, Volkmer A. 2009. Vibrational imaging based on stimulated Raman scattering microscopy. *New J. Phys.* 11:033026
77. Okada M, Smith NI, Palonpon AF, Endo H, Kawata S, et al. 2012. Label-free Raman observation of cytochrome *c* dynamics during apoptosis. *PNAS* 109(1):28–32
78. Ozeki Y, Umemura W, Otsuka Y, Satoh S, Hashimoto H, et al. 2012. High-speed molecular spectral imaging of tissue with stimulated Raman scattering. *Nat. Photon.* 6(12):845–51
79. Paige JS, Wu KY, Jaffrey SR. 2011. RNA mimics of green fluorescent protein. *Science* 333(6042):642–46
80. Pawley JB, Masters BR. 2008. Handbook of biological confocal microscopy. *J. Biomed. Opt.* 13:29902
81. Phelps ME. 2000. Positron emission tomography provides molecular imaging of biological processes. *PNAS* 97(16):9226–33

82. Piez K, Eagle H. 1958. The free amino acid pool of cultured human cells. *J. Biol. Chem.* 231:533–45
83. Ploetz E, Laimgruber S, Berner S, Zinth W, Gilch P. 2007. Femtosecond stimulated Raman microscopy. *Appl. Phys. B* 87(3):389–93
84. Potma EO, de Boeij WP, van Haastert PJM, Wiersma DA. 2001. Real-time visualization of intracellular hydrodynamics in single living cells. *PNAS* 98(4):1577–82
85. Potma EO, Xie XS. 2005. Direct visualization of lipid phase segregation in single lipid bilayers with coherent anti-Stokes Raman scattering microscopy. *ChemPhysChem* 6(1):77–79
86. Pully VV, Lenferink ATM, Otto C. 2011. Time-lapse Raman imaging of single live lymphocytes. *J. Raman Spectrosc.* 42(2):167–73
87. Radhakrishnan A, Goldstein JL, McDonald JG, Brown MS. 2008. Switch-like control of SREBP-2 transport triggered by small changes in ER cholesterol: a delicate balance. *Cell Metab.* 8(6):512–21
88. Raman CV, Krishnan KS. 1928. A new type of secondary radiation. *Nature* 121(3048):501–2
89. Rinia HA, Burger KNJ, Bonn M, Müller M. 2008. Quantitative label-free imaging of lipid composition and packing of individual cellular lipid droplets using multiplex CARS microscopy. *Biophys. J.* 95(10):4908–14
90. Rodrigues TB, Serrao EM, Kennedy BWC, Hu D-E, Kettunen MI, Brindle KM. 2013. Magnetic resonance imaging of tumor glycolysis using hyperpolarized ^{13}C-labeled glucose. *Nat. Med.* 20(1):93–97
91. Saar BG, Freudiger CW, Reichman J, Stanley CM, Holtom GR, Xie XS. 2010. Video-rate molecular imaging in vivo with stimulated Raman scattering. *Science* 330(6009):1368–70
92. Saar BG, Johnston RS, Freudiger CW, Xie XS, Seibel EJ. 2011. Coherent Raman scanning fiber endoscopy. *Opt. Lett.* 36(13):2396–98
93. Salzer R, Siesler HW, eds. 2009. *Infrared Raman Spectroscopic Imaging*. Hoboken, NJ: Wiley
94. Schaffer JE. 2016. Lipotoxicity: many roads to cell dysfunction and cell death: introduction to a thematic review series. *J. Lipid Res.* 57(8):1327–28
95. Shen Y, Xu F, Wei L, Hu F, Min W. 2014. Live-cell quantitative imaging of proteome degradation by stimulated Raman scattering. *Angew. Chem. Int. Ed.* 53(22):5596–99
96. Shen Y, Zhao Z, Zhang L, Shi L, Shahriar S, et al. 2017. Metabolic activity induces membrane phase separation in endoplasmic reticulum. *PNAS* 114(51):13394–99
97. Shi L, Shen Y, Min W. 2018. Visualizing protein synthesis in mice with in vivo labeling of deuterated amino acids using vibrational imaging. *APL Photon.* 3:092401
98. Silva WR, Graefe CT, Frontiera RR. 2016. Toward label-free super-resolution microscopy. *ACS Photon.* 3(1):79–86
99. Simons K, Sampaio JL. 2011. Membrane organization and lipid rafts. *Cold Spring Harb. Perspect. Biol.* 3(10):a004697
100. Simons K, Van Meer G. 1988. Lipid sorting in epithelial cells. *Biochemistry* 27(17):6197–202
101. Singer S, Nicolson GL. 1972. The fluid mosaic model of the structure of cell membranes. *Science* 175(23):720–31
102. Stiebing C, Meyer T, Rimke I, Matthäus C, Schmitt M, et al. 2017. Real-time Raman and SRS imaging of living human macrophages reveals cell-to-cell heterogeneity and dynamics of lipid uptake. *J. Biophoton.* 10(9):1217–26
103. Suhalim JL, Chung C-Y, Lilledahl MB, Lim RS, Levi M, et al. 2012. Characterization of cholesterol crystals in atherosclerotic plaques using stimulated Raman scattering and second-harmonic generation microscopy. *Biophys. J.* 102:1988–95
104. Surmacki J, Musial J, Kordek R, Abramczyk H. 2013. Raman imaging at biological interfaces: applications in breast cancer diagnosis. *Mol. Cancer* 12:48
105. Syed A, Smith EA. 2017. Raman imaging in cell membranes, lipid-rich organelles, and lipid bilayers. *Annu. Rev. Anal. Chem.* 10:271–91
106. Thurber GM, Yang KS, Reiner T, Kohler RH, Sorger P, et al. 2013. Single-cell and subcellular pharmacokinetic imaging allows insight into drug action in vivo. *Nat. Commun.* 4:1504
107. Tipping WJ, Lee M, Serrels A, Brunton VG, Hulme AN. 2016. Stimulated Raman scattering microscopy: an emerging tool for drug discovery. *Chem. Soc. Rev.* 45(8):2075–89

108. Tipping WJ, Lee M, Serrels A, Brunton VG, Hulme AN. 2017. Imaging drug uptake by bioorthogonal stimulated Raman scattering microscopy. *Chem. Sci.* 8(8):5606–15
109. Unger RH. 2002. Lipotoxic diseases. *Annu. Rev. Med.* 53:319–36
110. van Manen H-J, Lenferink A, Otto C. 2008. Noninvasive imaging of protein metabolic labeling in single human cells using stable isotopes and Raman microscopy. *Anal. Chem.* 80(24):9576–82
111. Villareal VA, Fu D, Costello DA, Xie XS, Yang PL. 2016. Hepatitis C virus selectively alters the intracellular localization of desmosterol. *ACS Chem. Biol.* 11(7):1827–33
112. Walker-Samuel S, Ramasawmy R, Torrealdea F, Rega M, Rajkumar V, et al. 2013. In vivo imaging of glucose uptake and metabolism in tumors. *Nat. Med.* 19(8):1067–72
113. Wang C, Han B, Zhou R, Zhuang X. 2016. Real-time imaging of translation on single mRNA transcripts in live cells. *Cell* 165(4):990–1001
114. Wang C-C, Moorhouse S, Stain C, Seymour M, Green E, et al. 2018. In situ chemically specific mapping of agrochemical seed coatings using stimulated Raman scattering microscopy. *J. Biophoton.* 11(11):e20180010
115. Wang P, Li J, Wang P, Hu C-R, Zhang D, et al. 2013. Label-free quantitative imaging of cholesterol in intact tissues by hyperspectral stimulated Raman scattering microscopy. *Angew. Chem. Int. Ed.* 52(49):13042–46
116. Weeks T, Schie I, den Hartigh LJ, Rutledge JC, Huser T. 2011. Lipid-cell interactions in human monocytes investigated by doubly-resonant coherent anti-Stokes Raman scattering microscopy. *J. Biomed. Opt.* 16(2):21117
117. Wei L, Chen Z, Shi L, Long R, Anzalone AV, et al. 2017. Super-multiplex vibrational imaging. *Nature* 544(7651):465–70
118. Wei L, Hu F, Chen Z, Shen Y, Zhang L, Min W. 2016. Live-cell bioorthogonal chemical imaging: stimulated Raman scattering microscopy of vibrational probes. *Acc. Chem. Res.* 49(8):1494–502
119. Wei L, Hu F, Shen Y, Chen Z, Yu Y, et al. 2014. Live-cell imaging of alkyne-tagged small biomolecules by stimulated Raman scattering. *Nat. Methods* 11(4):410–12
120. Wei L, Shen Y, Xu F, Hu F, Harrington JK, et al. 2015. Imaging complex protein metabolism in live organisms by stimulated Raman scattering microscopy with isotope labeling. *ACS Chem. Biol.* 10(3):901–8
121. Wei L, Yu Y, Shen Y, Wang MC, Min W. 2013. Vibrational imaging of newly synthesized proteins in live cells by stimulated Raman scattering microscopy. *PNAS* 110:11226–31
122. Wenk MR. 2005. The emerging field of lipidomics. *Nat. Rev. Drug Discov.* 4(7):594–610
123. Willmann JK, van Bruggen N, Dinkelborg LM, Gambhir SS. 2008. Molecular imaging in drug development. *Nat. Rev. Discov.* 7(7):591–607
124. Wu B, Eliscovich C, Yoon YJ, Singer RH. 2016. Translation dynamics of single mRNAs in live cells and neurons. *Science* 352(6292):aaf1084
125. Yamakoshi H, Dodo K, Okada M, Ando J, Palonpon A, et al. 2011. Imaging of EdU, an alkyne-tagged cell proliferation probe, by Raman microscopy. *J. Am. Chem. Soc.* 133(16):6102–5
126. Yamakoshi H, Dodo K, Palonpon AF, Fujita K, Kawata S, Sodeoka M. 2012. Alkyne-tag Raman imaging for visualization of mobile small molecules in live cells. *J. Am. Chem. Soc.* 134(51):20681–89
127. Yamakoshi H, Palonpon AF, Dodo K, Ando J, Kawata S, et al. 2014. Simultaneous imaging of protonated and deprotonated carbonylcyanide *p*-trifluoromethoxyphenylhydrazone in live cells by Raman microscopy. *Chem. Commun.* 50(11):1341–43
128. Yamakoshi H, Palonpon A, Dodo K, Ando J, Kawata S, et al. 2015. A sensitive and specific Raman probe based on bisarylbutadiyne for live cell imaging of mitochondria. *Bioorg. Med. Chem. Lett.* 25(3):664–67
129. Yan X, Hoek TA, Vale RD, Tanenbaum ME. 2016. Dynamics of translation of single mRNA molecules in vivo. *Cell* 165(4):976–89
130. Yu Y, Mutlu AS, Liu H, Wang MC. 2017. High-throughput screens using photo-highlighting discover BMP signaling in mitochondrial lipid oxidation. *Nat. Commun.* 8(1):865
131. Yu Y, Ramachandran PV, Wang MC. 2014. Shedding new light on lipid functions with CARS and SRS microscopy. *Biochim. Biophys. Acta* 1841(8):1120–29

132. Yue S, Li J, Lee S-Y, Lee HJ, Shao T, et al. 2014. Cholesteryl ester accumulation induced by PTEN loss and PI3K/AKT activation underlies human prostate cancer aggressiveness. *Cell Metab.* 19(3):393–406
133. Zeng C, Hu F, Long R, Min W. 2018. A radiometric Raman probe for live-cell imaging of hydrogen sulfide in mitochondria by stimulated Raman scattering. *Analyst* 143(20):4844–48
134. Zenobi R. 2013. Single-cell metabolomics: analytical and biological perspectives. *Science* 342(6163):1243259
135. Zhang C, Zhang D, Cheng J-X. 2015. Coherent Raman scattering microscopy in biology and medicine. *Annu. Rev. Biomed. Eng.* 17:415–45
136. Zhang D, Slipchenko MN, Cheng J-X. 2011. Highly sensitive vibrational imaging by femtosecond pulse stimulated Raman loss. *J. Phys. Chem. Lett.* 2(11):1248–53
137. Zhang D, Wang P, Slipchenko MN, Ben-Amotz D, Weiner AM, Cheng J-X. 2013. Quantitative vibrational imaging by hyperspectral stimulated Raman scattering microscopy and multivariate curve resolution analysis. *Anal. Chem.* 85(1):98–106
138. Zhang D, Wang P, Slipchenko MN, Cheng J-X. 2014. Fast vibrational imaging of single cells and tissues by stimulated Raman scattering microscopy. *Acc. Chem. Res.* 47(8):2282–90
139. Zhang D, Wang PP, Slipchenko MN, Cheng J, Leaird DE, et al. 2014. Breaking the diffraction limit by saturation in stimulated-Raman-scattering microscopy: a theoretical study. *Phys. Rev. A* 11(1):2641–43
140. Zhang J, Yan S, He Z, Ding C, Zhai T, et al. 2018. Small unnatural amino acid carried Raman tag for molecular imaging of genetically targeted proteins. *J. Phys. Chem. Lett.* 9(16):4679–85
141. Zhang L, Min W. 2017. Bioorthogonal chemical imaging of metabolic changes during epithelial-mesenchymal transition of cancer cells by stimulated Raman scattering microscopy. *J. Biomed. Opt.* 22(10):1–7
142. Zhang X, de Juan A, Tauler R. 2015. Multivariate curve resolution applied to hyperspectral imaging analysis of chocolate samples. *Appl. Spectrosc.* 69(8):993–1003
143. Zhao Z, Shen Y, Hu F, Min W. 2017. Applications of vibrational tags in biological imaging by Raman microscopy. *Analyst* 142(21):4018–29
144. Zumbusch A, Holtom GR, Xie XS. 1999. Three-dimensional vibrational imaging by coherent anti-Stokes Raman scattering. *Phys. Rev. Lett.* 82(20):4142–45

Annual Review of Biophysics
Volume 48, 2019

Contents